Fluctuating Curvature and Actuation in 4D Printed Asymmetric Networks by Frontal Photopolymerization

Advanced Materials Interfaces

ADVANCED MATERIALS INTERFACES Open Access

www.advmatinterfaces.de

RESEARCH ARTICLE OPEN ACCESS

Fluctuating Curvature and Actuation in 4D Printed Asymmetric Networks by Frontal Photopolymerization

Muhammad Ghifari Ridwan[1] | Zain Ahmad[1] | Alessandra Vitale[2] | João T. Cabral[1]

[1]Department of Chemical Engineering, Imperial College London, London, UK | [2]Department of Applied Science and Technology, Politecnico di Torino, Torino, Italy

Correspondence: João T. Cabral (j.cabral@imperial.ac.uk)

Received: 7 October 2025 | **Revised:** 15 December 2025 | **Accepted:** 15 December 2025

Keywords: 4D printing | asymmetric network | evaporation | diffusion | frontal photopolymerization

ABSTRACT

We investigate the spatiotemporal response of asymmetric polymer networks fabricated by frontal photopolymerization (FPP), a directional solidification process characterized by the emergence of conversion gradients and traveling waves, previously shown to support origami assembly. Employing a model system of UV cross-linking poly(ethylene glycol) diacrylate, we examine the frontal network conversion, the chemical exchanges during solvent development, and ensuing removal during drying. We find that the coupling of diffusion-evaporation and swelling-shrinkage processes gives rise to the formation of asymmetric 'skin' layers resulting in dynamic curvature fluctuations in otherwise planar beams, even in the absence of spatial patterning employed in FPP origami. Building on these findings, we demonstrate the fabrication of autonomous bistable switches and self-propulsion via a snapping instability that harness the environmental response of such ubiquitous asymmetric polymer networks.

1 | Introduction

Autonomous and origami-inspired material design has emerged as a powerful strategy for creating complex, functional structures [1–4], spanning multiple lengths and timescales, with applications ranging from soft robotics [5] and biomedical devices [6, 7] to adaptive architectural components [8, 9]. These approaches exploit the intrinsic physical and chemical properties of materials to achieve shape transformations, folding, in response to an external stimulus (e.g., light, thermal, electric, magnetic, or chemical) without the need for external mechanical forces [10–15]. Spontaneous assembly offers thus a route to creating functional and responsive architectures by programming local interactions, with geometric and temporal control by design.

Frontal photopolymerization (FPP) has emerged as a versatile and scalable approach to generate planar, multilevel and gradient polymer networks [16–18]. FPP is a class of photopolymerization processes for which, under conditions of strong light attenuation and limited mass and diffusion processes, a sharp traveling solidification front develops and propagates into the liquid monomer. While the spatiotemporal evolution of FPP networks can become complex, and even autocatalytic for highly exothermic processes, a range of photopolymer systems exhibit surprisingly simple kinetics with time-invariant, propagating, conversion profiles. FPP networks exhibit prescribed conversion gradients along the direction of propagation of light, which can be readily encoded by design [19]. This gradient structure imparts unique mechanical properties, such as spatially varying modulus and strain [20], which can drive complex, non-planar deformations without additional patterning steps or external forces [18, 21]. FPP enables thus the facile fabrication of asymmetric polymer networks, with modulated physical, mechanical and transport properties with exceptional potential for spontaneous material assembly [18, 22–25]. Such conversion gradients have been exploited in the design and fabrication of origami structures [23, 24], anchored on the

predictive control of optical attenuation, and conversion kinetics, which define the gradient of mechanical modulus and shrinkage strain [22, 23], generally associated with photopolymerization and development (i.e., the exposure to selective solvent and its subsequent removal). Prior work has exploited FPP to fabricate origami-inspired structures [18, 23], auxetic materials [26], and 4D architectures [21, 27], and equilibrium models have successfully described the dry and solvated configurations of such gradient networks [24].

Here, we examine the spatiotemporal response and kinetics of asymmetric networks fabricated by FPP, focusing on the evolution of pattern curvature over time. Specifically, we have observed that such networks can exhibit significant fluctuations in curvature, which we seek to understand and harness in practical applications for responsive and autonomous soft materials. We thus develop a coarse-grained model that describes the spatiotemporal evolution of the network conversion and optical attenuation, which we connect to the monomer-solvent exchange and removal, and its impact on network mechanics, shrinkage strain and the evolution of the neutral axis in the cross-section of the material, to compute the macroscopic curvature. Our experimental findings and minimal model elucidate the interplay between cross-linking, evaporation-diffusion, and stress distribution, establishing the conditions for a fluctuating curvature response. Based on this framework, we design autonomous functional structures, able to jump and switch configuration driven by the reponse of asymmetric FPP networks.

2 | Results

2.1 | FPP Network Formation

Under conditions of strong optical attenuation and limited mass and thermal diffusion processes, photopolymerization results in the formation of a travelling wavefront of network formation along the direction of light propagation, which is termed FPP [16, 19, 28, 29]. This directional solidification process provides a powerful and versatile approach to fabricating asymmetric polymer networks with prescribed conversion profiles, and thus spatially varying mechanical properties normal to the surface of the material. For our experiments, we select poly(ethylene glycol) diacrylate (PEGDA) as a model photosensitive network former and a conventional UV lithography system, as illustrated in Figure 1a. The FPP kinetics (Figure 1b) are well described by the coarse-grained model previously introduced by Cabral and co-workers [16, 17, 30, 31]. This minimal model provides a simple framework to describe the spatiotemporal evolution of the network conversion profile $\phi(z, t)$ emanating from the illuminated surface ($z = 0$) and changes in light intensity $I(z, t)$ during FPP, detailed in Section S1. Figure 1b plots the experimentally measured polymer film thickness z_f and optical attenuation coefficient $\bar{\mu}$ in terms of the UV irradiation dose d ($\equiv I(z = 0) \times t$) for the PEGDA system, as well as model predictions for 'photoinvariant' FPP, for which $\bar{\mu} \approx \mu(t = 0)$ remains largely unchanged (up to $d \approx 700$ mJcm^{-2}, above which photobleaching occurs). Under these conditions, the travelling conversion profile becomes shape-invariant in time (or dose),

$$\phi(z, d) = 1 - \exp[-Kd \exp(-\bar{\mu} z)] \tag{1}$$

where K is a characteristic conversion rate constant. The front position z_f (corresponding to the film thickness) is readily obtained by the intersection of $\phi(z, d)$ with a given critical conversion threshold ϕ_c required for solidification, yielding,

$$z_f(d) = \frac{\ln\left[\frac{Kd}{\ln\frac{1}{1-\phi_c}}\right]}{\bar{\mu}} \tag{2}$$

with the onset of film formation corresponding to the earliest time (or dose, $d_c = \frac{1}{K}\ln(\frac{1}{1-\phi_c})$) when this condition is met. Experimentally, the 'development' of the polymeric network by a selective solvent (ethanol in this work) truncates the $\phi(z, d)$ yielding a well defined polymer film of thickness z_f, as shown in Figure 1c. From FTIR measurements (see Section S2), we determine $\phi_c = 0.2$, and from self-consistent fitting of film growth and optical attenuation kinetics, we obtain $K = 0.029 \pm 0.004$ mJcm^{-2} and $\bar{\mu} = 3.4 \pm 0.1$ mm^{-1}, consistent with prior studies on FPP systems [18, 31].

2.2 | Emergence of Spontaneous Curvature in FPP Networks

Employing in-plane (xy) spatial modulation of light, for instance using greyscale photomasks, multiple exposures or direct writing, FPP can generate pseudo-3D structures [16] and enables the introduction of hinges and sheets, in otherwise planar photoconversion, that are amenable to origami assembly [18, 32]. However, even under uniform exposure, FPP encodes a prescribed network conversion gradient $\phi(z)$ along the direction of the propagation of light (i.e., normal to the material surface). This conversion gradient can non-trivially modulate the physical-chemistry of the network, including mechanics, shrinkage strains, solubility, and transport properties. Specifically, a gradient in Young's modulus and strain produces a differential stress across the network, resulting in a non-zero bending moment and the development of curvature, $\kappa \equiv 1/R$, where R is the radius of curvature [33]. Spontaneous curvature of asymmetric FPP networks is indeed observed experimentally. Intuitively, films should curve toward the illuminated film surface (if driven by a shrinkage strain that increases with cross-linking) or towards the less cross-linked face (if greater cross-linking reduces unrelaxed conversion strains), illustrated in Figure 1c. Gradient networks also exhibit complex response to vapor or solvent exposure and removal [23, 34], accompanied by swelling and shrinkage, significant changes of (spatially varying) mechanical properties, and sorption and diffusion properties [35, 36].

For the model PEGDA system investigated, we find that films exhibit positive curvature (i.e., curving away from the illuminated surface), once removed from the monomer bath and solvent-washed (developed), as illustrated in Figure 1d (and previously reported [18, 32]). Curvature κ varies strongly with irradiation dose, as shown in Figure 1e, and implicitly with z_f, as greater thickness leads to higher overall mechanical stiffness of the network (see Section S3). As expected, thicker polymeric slabs ($z_f \to \infty$) become planar ($\kappa \to 0$).

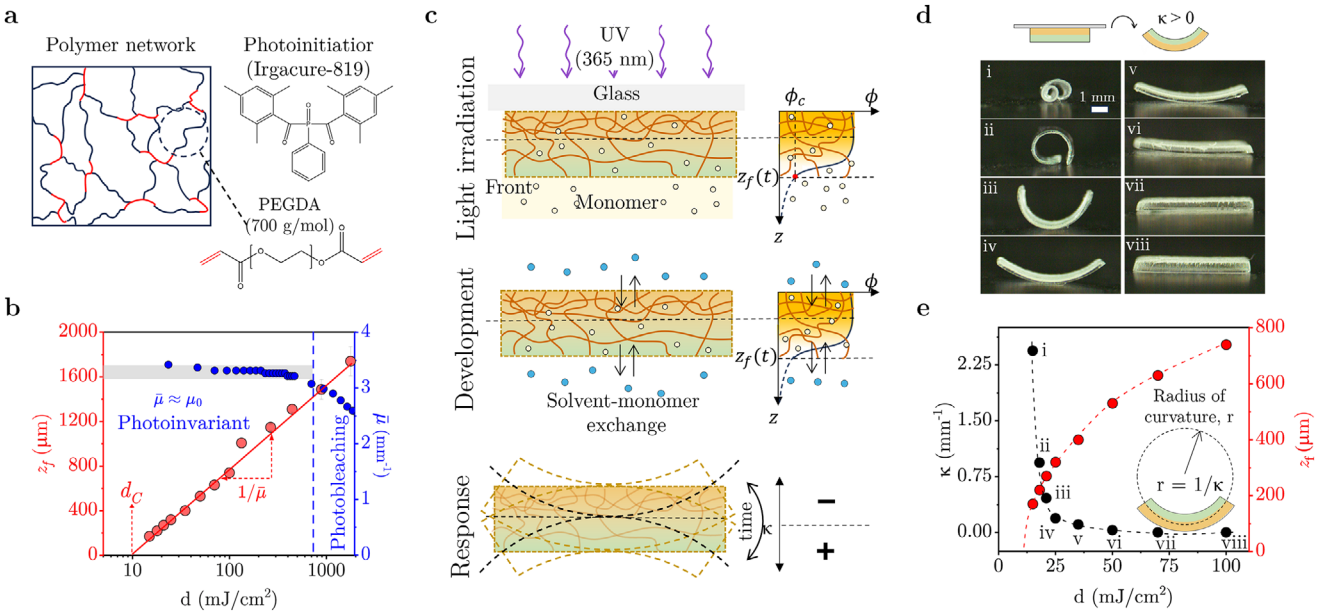

FIGURE 1 | Frontal photopolymerization of PEGDA and spontaneous emergence of curvature. (a) Schematic of PEGDA network (red illustrates cross-links). (b) Evolution of front position (z_f), corresponding to the network thickness, and composition-averaged optical attenuation ($\bar{\mu}$) with UV (365 nm) irradiation dose (d). The solid line corresponds to a fit to Equation (2), where d_C is a critical dose threshold; the vertical dashed line ($d \approx 700$ mJcm^{-2}) indicates the upper limit of photoinvariant behavior. (c) Schematic of the front propagation and evolution of the conversion profile $\phi(z)$, where ϕ_C is the critical conversion threshold for network formation (top panel); solvent-monomer exchange during development (middle); and spatiotemporal response of the gradient FPP network (bottom). (d) Long-time limit of the response of a photopolymerized beam (3×7 mm^2) with increasing d. (e) Dependence of beam curvature (κ), and corresponding thickness (z_f), as a function of irradiance dose d, for the FPP beams shown in (d).

2.3 | Fluctuating Curvature in FPP Networks

We find that, instead of a defined curvature associated with FPP conversion, κ fluctuates and changes sign, in a manner that is both time and process-dependent. In order to elucidate the nature of such curvature oscillations, we next examine the FPP conversion and development steps in detail. During polymerization, the FPP network is generally supported by a substrate, typically glass or a non-adhering material (such as polydimethylsiloxane (PDMS) or a teflon coating) and illumination is from the substrate side. During this process, the network grows into and remains immersed within its own monomer. Diffusion of monomer into (static and evolving) polymeric networks has been considered theoretical and experimentally [25], and has the potential to cause network swelling. In our experiments, however, we do not observe the emergence of film curvature during light exposure, neither on films supported to glass (strongly adhered), nor in PDMS (non/weakly-adhered). Subsequently, the FPP network film is removed from the monomer bath and detached from the substrate. At this stage, curvature can be observed, which we associate with the removal of uncrosslinked monomer within the network. Curvature is positive ($\kappa > 0$), i.e. toward the less cross-linked face of the film. In order to 'develop' the FPP network, and remove the monomer, the material is then immersed in a selective solvent (such as ethanol) to enable monomer-solvent exchanges. These exchanges can drive curvature fluctuations from positive to negative and then positive again. After development, excess solvent is carefully removed with a pad, and the polymer network is allowed to dry at ambient conditions. Similarly, this network drying process leads to the emergence of curvature fluctuations, from approximately flat, to negative, and then positive.

To illustrate and quantify these curvature fluctuations, we employ a 5-leaf photomask pattern (a mm-scale 'starfish') and pattern a PEGDA network onto glass, which is then carefully removed and developed/immersed in ethanol for 3 min, as illustrated in Figure 2a. The immersion time was selected based on the solvent absorption kinetics of the asymmetric polymer network (Figure 2a; Figure S9), corresponding to the point at which the absorbed solvent mass approaches its asymptotic value. Fluctuation data are robust for solvent development times of 3 min or longer (Sections S4 and S5). After development, the polymer networks are pad dried to remove solvent excess at the surface; evidently this process can introduce some variability in the subsequent curvature response of the network and we have thus examined its role (Section S6). In short, while the extent of pad drying can impact the kinetics of the network response, a broad range of conditions yield robust and repeatable outcomes. We select a pattern thickness of $z_f = 200$ #x000B5;m (guided by Figure 1e), corresponding to a UV dose of 15.2 mJcm^{-2} and terminal curvature $\kappa \approx 0.45$ mm^{-1}. The network conversion profile $\phi(z)$ (Figure 2b) yields a gradient between $\phi(z = 0) \approx 0.37$ at the illuminated surface, and $\phi(z_f) \equiv \phi_c \approx 0.2$ at the solid–liquid interface.

The asymmetric network immersed in ethanol exhibits a slight positive curvature, before it is transferred to the drying stage, where $\kappa \approx 0$ initially. The spontaneous evolution of κ is shown in Figure 2c, and pattern gradually bends into a convex shape, $\kappa < 0$ (toward the face of greater ϕ), and then reverses into a concave shape, $\kappa > 0$ (away from the plane), over timescales of seconds to minutes. Asymptotically, the pattern approaches $\kappa \approx 0.5$ mm^{-1}, in a closed flower configuration. The corresponding optical images

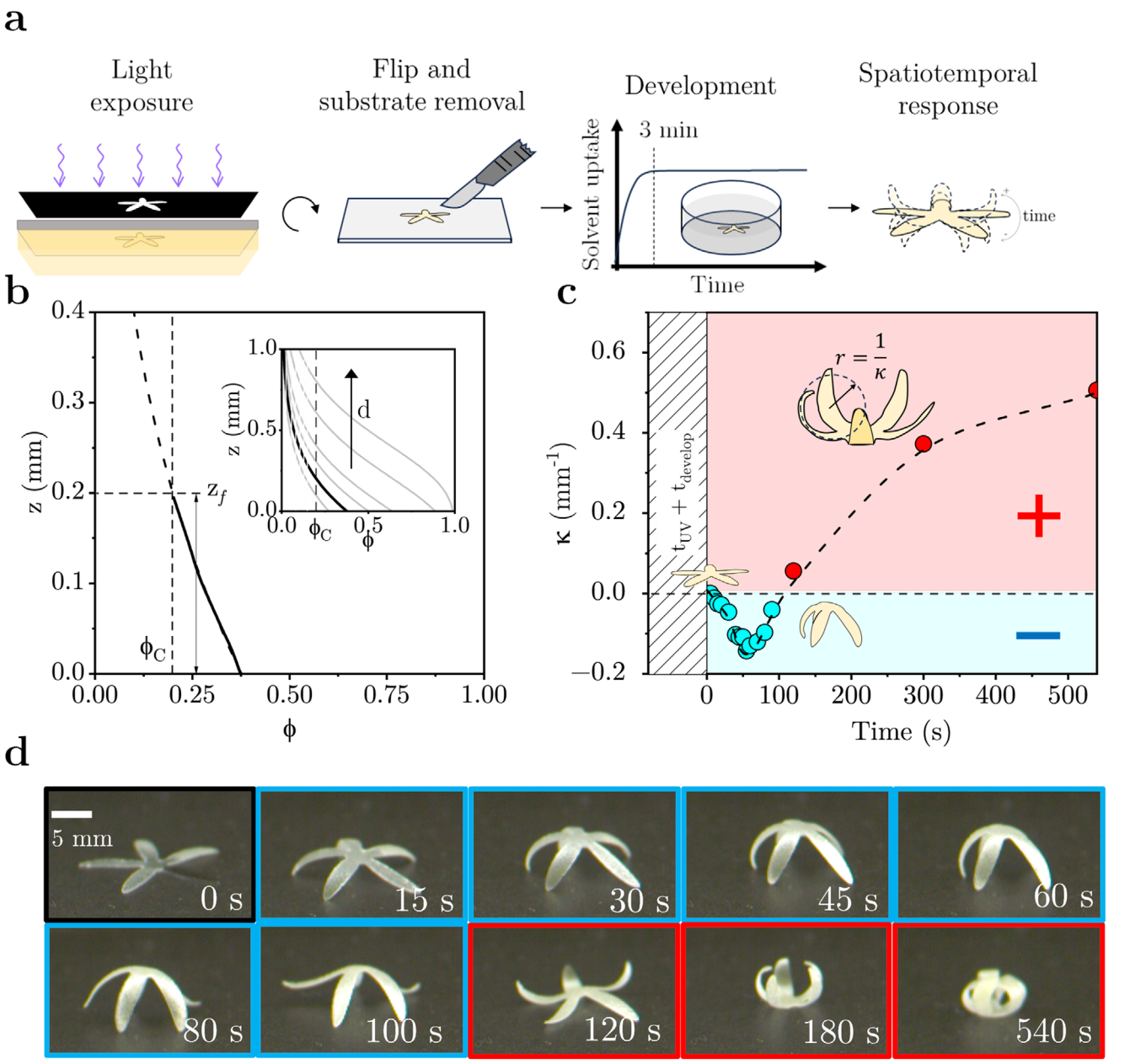

FIGURE 2 | Spatiotemporal response of a gradient FPP pattern. (a) Fabrication process of a 4D FPP structure, including light exposure, 'development' (i.e., solvent immersion for 3 min, reaching asymptotic uptake), and spatiotemporal response. (b) Photopolymerization profile $\phi(z)$ at fixed irradiance dose (d), yielding a gradient network with thickness z_f. Inset illustrates traveling waves of network formation with increasing d. (c) Evolution of pattern curvature following development, from an initial negative (blue) to positive (red) κ over time (shown for $z_f = 0.2$ mm). (d) Corresponding optical time-sequenced images of the 4D FPP pattern, color-coded according to their curvature.

are shown in Figure 2d. This spatiotemporal response of the polymer network is robust to changing the FPP support, for instance from glass to PDMS, inverting the illumination geometry (top-down to bottom-up, with respect to buoyancy) as detailed in (Section S7). While substrate adhesion could potentially influence curvature fluctuation dynamics due to differing residual stress [18, 37, 38], under the network-forming conditions that support curvature fluctuations ($\Delta\phi \approx 0.2$) we observe minimal impact on curvature dynamics (Section S7 and Figure S8). We thus conclude that the fluctuations are not impacted by substrate adhesion. As expected, restricting mass transfer or exerting an adhesive force at one interface (e.g., by not removing the substrate) quantitatively changes the curvature dynamics (Section S8).

The sequential transformations experienced by asymmetric polymer networks appear thus to be related to the evolution of internal stress distribution during solvent exchange and drying, transient differential shrinkage, and changes in mechanical properties across the network conversion gradient. Understanding and controlling these are required to program shape-morphing behavior and function by design.

2.4 | A Minimal Model for Diffusion-Evaporation and Spontaneous Curvature Fluctuations in an FPP Asymmetric Network

With these ideas in mind, we consider a solvated FPP network and write Fick's 2nd law to describe the diffusion of solvent within the polymer matrix and its surface evaporation,

$$\frac{\partial C(z,t)}{\partial t} = \frac{\partial}{\partial z}\left(D_e \frac{\partial C(z,t)}{\partial z}\right) \tag{3}$$

where $C(z, t)$ is the solvent concentration along the polymer network, D_e is an 'effective' diffusion constant, and t is time following exposure to ambient air. We impose appropriate boundary conditions at both interfaces, $z = 0$ (illuminated surface) and $z = z_f$ (solid–liquid interface),

$$-D_e \frac{\partial C(z,t)}{\partial z}\bigg|_{z=0} = k_{evap}[C(0,t) - C_{air}] \tag{4}$$

$$-D_e \frac{\partial C(z,t)}{\partial z}\bigg|_{z=z_f} = -k_{evap}[C(z_f,t) - C_{air}] \tag{5}$$

where k_{evap} is an evaporation rate constant, and C_{air} is the solvent concentration in air, which can be neglected (≈0) for simplicity (corresponding to a well ventilated environment). We define the initial solvent concentration profile $C(z, t = 0)$ based on solvent mass uptake ($m_{solvent}$) experiments (See Section S4) and assume a simple relation between conversion $\phi(z, t)$ and solvent uptake to solve $m_{solvent} = \int_0^{z_f} C_0 \phi^{-n} dz$ and set constant C_0, which define $C(z, 0) = C_0 \times \phi^{-n}$, where n is a parameter for polymer absorption capacity power law exponent to define initial condition.

To correlate the solvent uptake/loss with mechanical properties, we introduce a reduced parameter termed evaporation ratio $\eta_{evap} \equiv C(z, t)/C(z, 0)$, defined as the ratio of evaporated solvent concentration to initial solvent concentration; the network has thus $\eta_{evap} = 0$ in its dry state, and $\eta_{evap} = 1$ when fully swollen. We then introduce an empirical relation between the Young's modulus (E) and strain (ε) of the swollen and dried gradient network, in terms of ϕ and η_{evap}. The lowest value of E corresponds to the critical conversion threshold [37], ϕ_c, which we denote E_0. We then relate strain to η_{evap},

$$\varepsilon(z,t) = [\varepsilon_{swell}(\phi) - \varepsilon_{dry}(\phi)]\eta_{evap}(z,t) + \varepsilon_{dry}(\phi) \tag{6}$$

returning limiting cases $\varepsilon = \varepsilon_{dry}$ or ε_{swell} for $\eta_{evap} = 0$ or 1, respectively, which depend on polymer-solvent interactions, and has been reported for some solvents [23]. We describe the spatiotemporal evolution of the mechanical modulus following

$$E(z,t) = E_0 + [E_{c,swollen}(\phi_c, \eta_{evap} = 1) + (E_{c,dry} - E_{c,swollen})(1 - \eta_{evap})^{n_1}][\phi_{conv} - \phi_{c,conv}]^{n_2} \tag{7}$$

where E_0 is the Young's modulus of the network formed during photopolymerization upon reaching ϕ_c [37], and n_1 and n_2 correspond to power law exponents for η_{evap} and ϕ. Equation (7) returns the equilibrium value of $E = E_0 + E_{swell}(\phi - \phi_c)^{n_2}$ and $E = E_0 + E_{dry}(\phi - \phi_c)^{n_2}$ for $\eta_{evap} = 0$ and 1, respectively, which has been reported by others [18, 23, 37]. Equations (6) and (7) enable a straightforward calculation of the curvature κ due to the solvent evaporation-diffusion according to Bernoulli's beam theory [33, 39],

$$\kappa(t) = \frac{\int_0^h E(z,t)\varepsilon(z - z_N(t), t)dz}{\int_0^h E(t)(z - z_N(t))^2 dz} \tag{8}$$

where the position of the neutral axis,

$$z_N(t) = \frac{\int_0^h E(z,t) z dz}{\int_0^h E(z,t) dz}, \tag{9}$$

also evolves during the process. An illustration of the model results (parameters tabulated in Section S9 and Table S1) is provided in Figure 3 for (a) the solvent concentration profile $C(z, t)$, (b) stress distribution $\sigma \equiv E\varepsilon$ (considering $\sigma_{z=z_N} = 0$, with η_{evap} in insert), and finally (c) the curvature evolution $\kappa(t)$, showing good agreement with experimental observations. Details of the minimal model, underlying assumptions and parameterization are provided in Section S9.

2.5 | Transient Thin Films Drive the Curvature Fluctuation

A simple physical picture emerges naturally from our simulation results. Upon initial exposure to ambient conditions, solvent evaporates rapidly at both film interfaces, creating thin regions of solvent depletion, or drier 'skins', indicated by the orange shading in Figure 3a. The $C(z, t)$ profile is asymmetric, following from the gradient conversion profile $\phi(z, t)$, yielding an asymmetric skin width at both interfaces. A strong dependence of $E(\phi)$ results in a large asymmetry in compressive interfacial stress $\sigma(z)$ within the drying polymer network (Figure 3b), which are greatest near the illuminated surface ($z = 0$) thus resulting in an initial bending with $\kappa < 0$, toward that facet. As drying proceeds, the solvent within the network diffuses toward both interfaces, causing a gradual increase in stiffness throughout the structure. Simultaneously, the neutral axis z_N also shifts during drying (Figure 3b), and the non-monotonic evolution of compressive to tensile stress $\sigma(z, t)$ causes the upper section of the slab to undergo a greater relative change with respect to the bottom section, resulting in a curvature reversal at a defined timescale. The final curvature reaches a network-dependent asymptote, $\kappa > 0$, as the internal stress distribution equilibrates over time (Figure 3c). In simple terms, this curvature fluctuation is caused by the simultaneous displacement of the neutral axis during the asymmetric drying process, accompanying the evolution of the mechanical properties of the network propagating from the skin layers: the overall stress distribution leads to an initially negative net stress, which then becomes a net positive stress, yielding a change in sign of the bending moment (detailed in Section S9).

In order to design the curvature fluctuation profile, we consider the FPP model parameters, and recall that the optical attenuation coefficient $\bar{\mu}$ effectively defines the interfacial profile $\phi(z)$ of the traveling photopolymerization wave. We consider two additional (extreme) cases, namely $\bar{\mu}$: 0.77 and 16.8 mm^{-1} (Figure 3c), in addition to 3.4 mm^{-1} employed so far, and photopolymerize

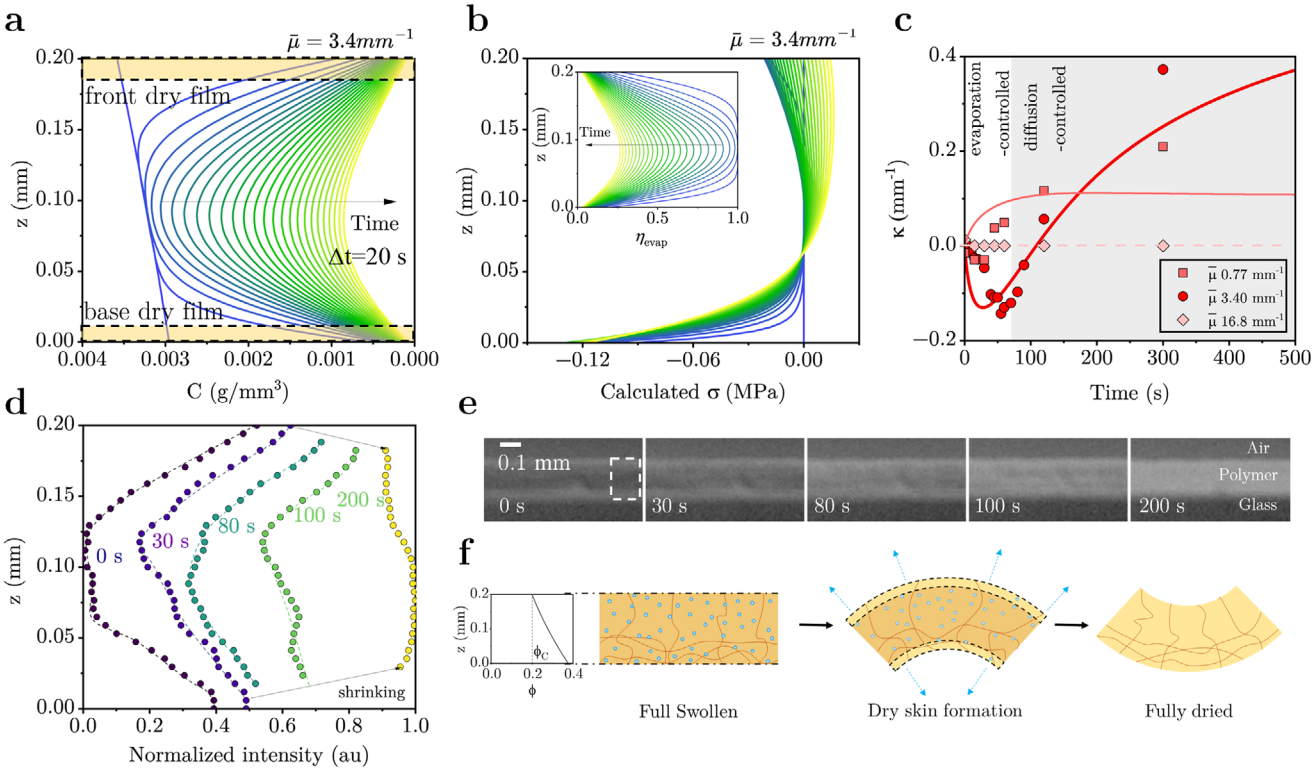

FIGURE 3 | Minimal (1D) Simulation of Spatiotemporal Response of FPP Network following development. (a) Evolution of developing solvent concentration $C(z, t)$ and (b) network stress (σ) with with z and t (see text). The inset shows the calculated evolution of η_{evap}. (c) Computed and experimentally-measured κ from the data in Figure 2, and by varying $\bar{\mu}$. (d) Optical measurement of intensities of networks during drying process. (e) Optical images of networks during the drying process. (f) Schematic of the mechanism underpinning the curvature fluctuation, indicating the network swollen by solvent (during development); the asymmetric formation of transient skins at both interfaces; and the fully dried network.

beams imposing the same thickness $z_f = 0.2$ mm. At low $\bar{\mu}$, curvature fluctuations are suppressed and κ increases monotonically with time. This arises from the shallow $\phi(z)$ gradient ($\Delta\phi \equiv \phi(z = 0) - \phi(z_f) \approx 0.03$), which causes the compressive stress difference between the base and front interfacial stress to be comparatively small (with respect to $\Delta\phi \approx 0.16$ for $\bar{\mu} = 3.4$ mm^{-1}). At the other extreme, for large high $\bar{\mu}$, the curvature effectively vanishes and $K \approx 0$, as the cross-sectional profile $\phi(z)$ approaches a step function (with $\phi(z = 0) \approx 1$, $\Delta\phi \approx 0.8$), and the large bending stiffness near $z = 0$, prevents the entire structure to bend. This explanation is consistent with observations from samples of a range of thicknesses z_f (Section S10). At sufficiently large thicknesses, the increased bending stiffness suppresses the development of bending structures and inhibits the emergence of curvature fluctuations.

To experimentally confirm the transient drying profile of the asymmetric film, we optically inspected the network during drying process to estimate the scattered light intensity across the interface, shown in Figure 3d,e. The measurements corroborate the formation of the two skin layers, at both interfaces, and their asymmetric evolution toward a full dried network (by analogy to the model predictions in Figure 3a). The proposed curvature fluctuation mechanism is illustrated in Figure 3f, starting from a planar solvent-swollen network (following development), a transient $\kappa < 0$ (toward greater ϕ) and reversal to $\kappa > 0$ as drying proceeds. Details of the model results are provided in Section S10 and Figure S17.

2.6 | Functional Materials by FPP Networks

Building on our experimental and simulation results, we develop a series of simple asymmetric FPP network structures capable of autonomous function and motion (Figure 4, detailed in Section S11 and Figure S19). Figure 4a shows the design of a trapezoidal beam with a short edge intended to undergo snapping and a rotational jump during curvature reversal, whose mechanism is depicted in the schematic. The red and green faces indicate high and low ϕ, respectively. During the first stage, the beam curves during evaporation ($\kappa < 0$), and stores elastic energy as the trapezium edges experience friction with the substrate and the network becomes anchored; upon curvature reversal ($\kappa > 0$), the network depins from the substrate, and this rapid energy release leads to snapping and a rotational jump in the direction of the short edge of the trapezium within ms timescales (Figure 4b and Video S1). Figure 4c depicts a mounted asymmetric network, shaped as a rectangular beam, whose edges are pinned to a rigid frame. Upon solvent immersion, the beam swells and elongates, developing a pre-set curvature κ ($\approx$0.13 mm^{-1} locally) whose sign can be selected manually. In both cases ($\kappa > 0$ and $\kappa < 0$), a series of forward and reverse traveling waves emerged along the profile; in the case of high to low ϕ, the assembly undergoes a snapping transition and changes curvature, while in the opposite architecture leads to structural failure through beam breakage (acting as a 'break switch') (Figure 4d; Video S2, and Video S3). The traveling profiles and event outcome is depicted in the panel below.

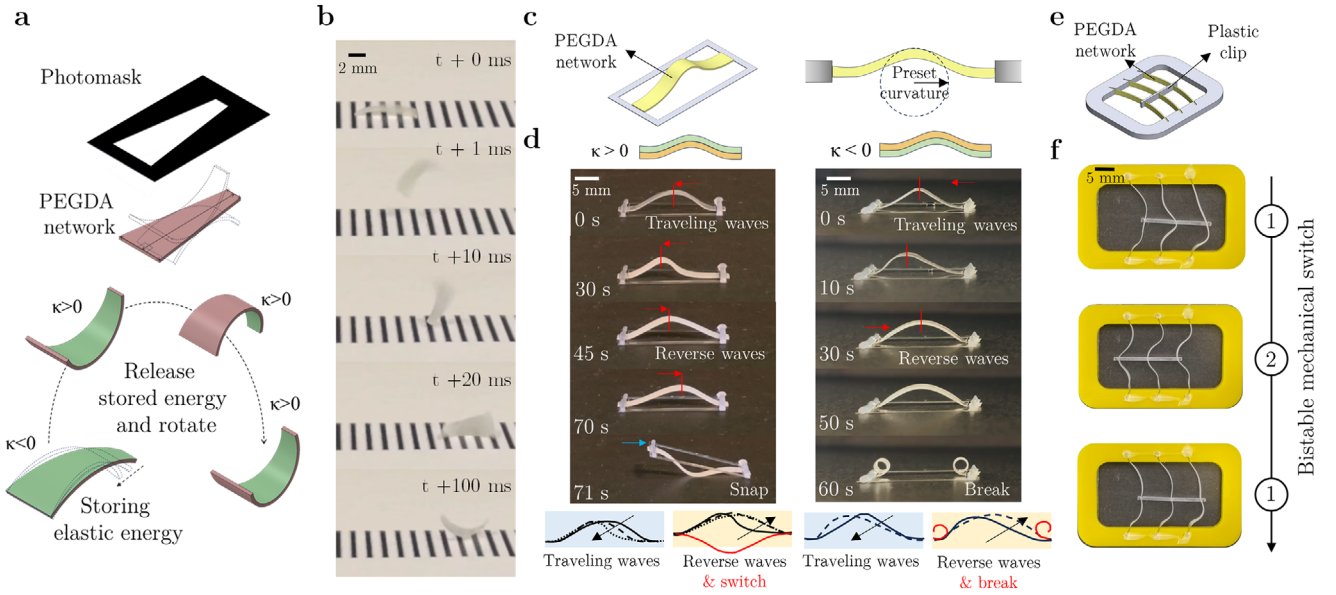

FIGURE 4 | Actuation and autonomous motion driven by the evaporation-diffusion mechanism in FPP network. (a) Schematic of the fabrication of an asymmetric FPP trapezoidal beam. (b) Autonomous snapping of trapezoidal beam: elastic energy is stored during the first stage (evaporation-controlled), followed by snapping and rotational jump, resulting into net displacement. (c) Schematic of a curved beam mounted on a rigid frame yielding (d) propagating wave motion resulting from beam curvature change and switch, accompanied by net displacement. Depending on how the asymmetric FPP beam is mounted, the beam switches configuration ($\kappa > 0$) conversion at the end of the cycle, or instead snaps ($\kappa < 0$) in the opposite polarity, creating a break switch. (e) Design of a bistable mechanical switch, illustrated with (f) sequential switching between bistable states: position ① → ② → ①.

Finally, we design a bistable mechanical switch by attaching three network beams mounted on the grooves on a rigid frame (Figure 4e). The initial curvature of the beam is dictated by the direction of the grooves, and the beams are linked via a central clip to enable synchronized actuation. Following solvent immersion and drying, the bistable switch demonstrates autonomous transitions between two stable positions in a repeatable sequence (Figure 4f; Video S4), demonstrating the potential for programmable mechanical logic.

3 | Discussion

Overall, we demonstrate how asymmetric networks generated by frontal photopolymerization (FPP) spontaneously undergo dynamic curvature fluctuations induced by exchanges of monomer or (developing) solvent at both interfaces. While the development of curvature in an asymmetric network can be expected and extensively observed experimentally (associated with a non-uniform distribution of shrinkage stresses), the emergence of curvature oscillations appears non-trivial to us. We have therefore examined theoretical and experimentally the FPP photoconversion of a model PEGDA network. We considered all steps, often implicit, in generating the polymer network, including: the formation of a network-monomer interface as the solidification wave propagates into the liquid; the subsequent exchanges between solvent (developer) and the uncross-linked monomer; and the evaporation of solvent that eventually results in the (dry) polymer network. We find that curvature oscillations occur due to imbalanced exchanges across the opposite interfaces of the asymmetric network. We observe a reproducible sequence of curvature changes, from flat ($\kappa \approx 0$) to convex ($\kappa<0$, curving towards greater ϕ) and then concave ($\kappa>0$, towards lower ϕ) during asymmetric evaporation, film formation, and shifting of the neutral axis as the internal stress distribution evolves.

In order to exploit these, a judicious design of the conversion profile $\phi(z, t)$ is required, and we find that our minimal FPP model provides an effective design framework for the layer thickness and conversion gradient. To rationalize and predict the oscillatory behavior, we introduce a coarse-grained model that incorporates polymer conversion, optical attenuation, and solvent transport (at the interfaces and within the bulk). This simple framework captures the essential mechanisms driving the observed shape morphing behavior and offers a predictive tool for designing responsive materials such as autonomous motion, which we illustrate with a rapid rotational jump, autonomous switches and bistable devices based on FPP asymmetric networks. By varying the interfacial profile, via irradiation dose, FPP kinetics or light attenuation, we can encode the profile of network asymmetry that governs time-dependent curvature transformations. Our findings establish a direct connection between photoconversion gradients and macroscopic actuation behavior, paving the way for programmable soft structures in 4D printing, soft robotics, and adaptive systems.

4 | Materials and Methods

4.1 | Chemicals

Polymer networks were fabricated by curing a mixture of polyethylene glycol diacrylate (PEGDA, M_n 700 g mol^{-1},

Sigma–Aldrich, code 455008) and photoinitiator phenylbis(2,4,6-trimethylbenzoyl)phosphine oxide (Irgacure-819, BASF, code 30128871). Mixtures of PEGDA with 0.67 % mass fraction were stirred at 500 rpm for 1 h, and stored at 4°C wrapped in aluminum foil (to prevent inadvertent photoinitiation) prior to use.

4.2 | Photopolymerization

The liquid mixture was placed between two microscope glass slides (1 inch × 3 inch, Fisherbrand 1238-3118) separated by a 1 mm glass spacer. Photomasks were designed on AutoCAD (2024) and printed on overhead projector (OHP) films using a laser printer at 600 dpi resolution, and placed atop the upper glass slide. Ultraviolet (UV) exposure was performed with a light source (Omnicure S1500) equipped with a 365 nm filter and irradiance 2.0–2.5 Wcm^2. Prior to each exposure, the UV light intensity was calibrated using a VItec RS-365 digital radiometer (Spectroline), along with measurements of the optical attenuation coefficients of the glass slides and photomask to compute accurate irradiation doses for each sample. A typical irradiation dose of 15.5 $mJcm^{-2}$ was employed to fabricate films of 0.2 mm thickness, with optical attenuation of 3.4 mm^{-1}, and doses up to 2000 $mJcm^{-2}$ were employed to characterize FPP kinetics, yielding film thicknesses between 0.1 and 1.7 mm. Typical beam dimensions were 7 × 3 mm^2. Following photopolymerization, the polymeric network was removed from the glass substrate with a scalpel and pad-dried to eliminate excess surface monomer. The samples were then immersed in ethanol (VWR Chemicals 99.7%, code 20821.321) for 3 min, used as a developing solvent, removed using tweezers, and pad-dried again to remove residual solvent. The resulting network was then imaged using a BASLER acA640-750uc camera equipped with a 0.5–1X Edmund Optics lens (87535).

4.3 | Starfish, Jumping, and Snapping Polymer Beam Fabrication

Various shapes were fabricated by designing an appropriate photomask, including 'starfish' (5 arms of 8 mm length and 2 mm width, detailed in Supporting Information), trapezoidal prism (bases length of 3 and 1 mm, and length 7 mm), beam-on-frame (2.5 mm width and length 18 mm); the bistable switch experiments employed a beam of 27 mm length and 2.5 mm width. All specimens had 0.2 mm thickness, and were fabricated as described above. For snapping instability experiments, prior to solvent development, the polymer samples were glued (Hot glue gun Tilswall W101 and Hot glue sticks Jelken HGS 1) onto a plastic frame (22 mm long, 12 mm wide, 2 mm frame width, 100 #x000B5;m thick acetate sheet). Bistable mechanical switch experiments were carried out by mounting three polymeric beams onto a polymethyl methacrylate frame (PMMA, AMARI Plastics 3 mm thickness), cut using a CO_2 laser (Universal Laser Systems); the central beam was also cut from PMMA (22 mm long, DRERIO 1 mm thickness)

4.4 | Material Characterization

Sample thickness was measured using a digital caliper (Mitutoyo, PK-0505CPX). Solvent absorption was quantified using a precision weighing balance (Mettler AE50). The beam images were captured with pylon software, and the curvature measurements were made with ImageJ software. For thin film visualization during drying, a 0.2 mm-thick photopolymer network was prepared on a glass substrate, immersed in ethanol for 3 min and subsequently dried under ambient conditions fixed onto the glass substrate (to ensure planarity) and imaged using a BASLER acA640-750uc camera with a 5X Mitutoyo lens (WD43373618). Infrared spectra were recorded using an INVENIO-S FTIR spectrometer (Bruker) equipped with a DTGS detector and Platinum ATR accessory. Each spectrum was acquired by averaging 32 single-beam scans with a 4 cm^{-1} resolution over a range of 4000 to 600 cm^{-1}. A clean, dry diamond crystal was used for background correction. All spectra underwent baseline correction using OPUS 8.5 software, with no additional data processing.

Acknowledgements

The authors acknowledged funding from EPSRC (EP/X030938/1) and the EU Horizon 2021-2027 programme under the Marie Skłodowska-Curie Doctoral Networks (MSCA-DN) grant agreement No 101073432 (ESPERANTO). JTC thanks the Royal Academy of Engineering (RCSRF1920/10/60) for funding a Research chair. The authors thank Hisay Lama, Liva Donina, Luis Torquato and Gunjan Tyagi for useful discussions and assistance with FTIR spectroscopy and imaging of drying films.

Conflicts of Interest

The authors declare no conflicts of interest.

Data Availability Statement

The data that support the findings of this study are available from the corresponding author upon reasonable request.

References

1. S. Leanza, S. Wu, X. Sun, H. J. Qi, and R. R. Zhao, "Active Materials for Functional Origami," *Advanced Materials* 36, no. 9 (2024): 2302066.

2. S. Felton, M. Tolley, E. Demaine, D. Rus, and R. Wood, "A Method for Building Self-Folding Machines," *Science* 345, no. 6197 (2014): 644–646.

3. D. H. Kim, S. Kim, S. R. Park, N. X. Fang, and Y. T. Cho, "Shape-Deformed Mushroom-Like Reentrant Structures for Robust Liquid-Repellent Surfaces," *ACS Applied Materials & Interfaces* 13, no. 28 (2021): 33618–33626.

4. B. Y. Ahn, D. Shoji, C. J. Hansen, E. Hong, D. C. Dunand, and J. A. Lewis, "Printed Origami Structures," *Advanced Materials* 22, no. 20 (2010): 2251–2254.

5. K. Hu, K. Rabenorosoa, and M. Ouisse, "A Review of SMA-Based Actuators for Bidirectional Rotational Motion: Application to Origami Robots," *Frontiers in Robotics and AI* 8 (2021): 678486.

6. S. R. Dabbagh, M. R. Sarabi, R. Rahbarghazi, E. Sokullu, A. K. Yetisen, and S. Tasoglu, "3D-Printed Microneedles in Biomedical Applications," *iScience* 24, no. 1 (2021): 102012.

7. D. Han, R. S. Morde, S. Mariani, et al., "4D Printing of a Bioinspired Microneedle Array with Backward-Facing Barbs for Enhanced Tissue Adhesion," *Advanced Functional Materials* 30, no. 11 (2020): 1909197.

8. A. Sydney Gladman, E. A. Matsumoto, R. G. Nuzzo, L. Mahadevan, and J. A. Lewis, "Biomimetic 4D Printing," *Nature Materials* 15, no. 4 (2016): 413–418.

9. Y. Zhang, F. Zhang, Z. Yan, et al., "Printing, Folding, and Assembly Methods for Forming 3D Mesostructures in Advanced Materials," *Nature Reviews Materials* 2, no. 4 (2017): 17019.

10. G. Fei, C. Parra-Cabrera, K. Zhong, K. Clays, and R. Ameloot, "From Grayscale Photopolymerization 3D Printing to Functionally Graded Materials," *Advanced Functional Materials* 34, no. 32 (2024): 2314635.

11. M. Z. Miskin, A. J. Cortese, K. Dorsey, et al., "Electronically Integrated, Mass-Manufactured, Microscopic Robots," *Nature* 584, no. 7822 (2020): 557–561.

12. M. Z. Miskin, K. J. Dorsey, B. Bircan, et al., "Graphene-Based Bimorphs for Micron-Sized, Autonomous Origami Machines," *Proceedings of the National Academy of Sciences* 115, no. 3 (2018): 466–470.

13. S.-J. Ahn, H. Lee, and K.-J. Cho, "3D Printing with a 3D-Printed Digital Material Filament for Programming Functional Gradients," *Nature Communications* 15, no. 1 (2024): 3605.

14. Y. Yao, A. M. Wilborn, B. Lemaire, et al., "Programming Liquid Crystal Elastomers for Multistep Ambidirectional Deformability," *Science* 386, no. 6726 (2024): 1161–1168.

15. L. Yue, X. Sun, L. Yu, et al., "Cold-Programmed Shape-Morphing Structures Based on Grayscale Digital Light Processing 4D Printing," *Nature Communications* 14, no. 1 (2023): 5519.

16. J. T. Cabral, S. D. Hudson, C. Harrison, and J. F. Douglas, "Frontal Photopolymerization for Microfluidic Applications," *Langmuir* 20, no. 23 (2004): 10020–10029.

17. J. T. Cabral and J. F. Douglas, "Propagating Waves of Network Formation Induced by Light," *Polymer* 46, no. 12 (2005): 4230–4241.

18. Z. Zhao, J. Wu, X. Mu, H. Chen, H. J. Qi, and D. Fang, "Origami by Frontal Photopolymerization," *Science Advances* 3, no. 4 (2017): e1602326.

19. M. G. Hennessy, A. Vitale, O. K. Matar, and J. T. Cabral, "Controlling Frontal Photopolymerization with Optical Attenuation and Mass Diffusion," *Physical Review E* 91, no. 6 (2015): 062402.

20. A. Vitale, M. G. Hennessy, O. K. Matar, and J. T. Cabral, "Interfacial Profile and Propagation of Frontal Photopolymerization Waves," *Macromolecules* 48, no. 1 (2015): 198–205.

21. Q. Zhang, X. Kuang, S. Weng, et al., "Rapid Volatilization-Induced Mechanically Robust Shape-Morphing Structures toward 4D Printing," *ACS Applied Materials & Interfaces* 12, no. 15 (2020): 17979–17987.

22. J. Wang, N. Dai, C. Jiang, et al., "Programmable Shape-Shifting 3D Structures via Frontal Photopolymerization," *Materials & Design* 198 (2021): 109381.

23. Z. Zhao, J. Wu, X. Mu, H. Chen, H. J. Qi, and D. Fang, "Desolvation-Induced Origami of Photocurable Polymers by Digital Light Processing," *Macromolecular Rapid Communications* 38, no. 13 (2017): 1600625.

24. Z. Zhao, H. J. Qi, and D. Fang, "A Finite Deformation Theory of Desolvation and Swelling in Partially Photo-Cross-Linked Polymer Networks for 3D/4D Printing Applications," *Soft Matter* 15, no. 5 (2019): 1005–1016.

25. M. G. Hennessy, A. Vitale, O. K. Matar, and J. T. Cabral, "Monomer Diffusion into Static and Evolving Polymer Networks during Frontal Photopolymerization," *Soft Matter* 13, no. 48 (2017): 9199–9210.

26. M. Lei, W. Hong, Z. Zhao, et al., "3D Printing of Auxetic Metamaterials with Digitally Reprogrammable Shape," *ACS Applied Materials & Interfaces* 11, no. 25 (2019): 22768–22776.

27. J. Wu, Z. Zhao, X. Kuang, C. M. Hamel, D. Fang, and H. J. Qi, "Reversible Shape-Change Structures by Grayscale Pattern 4D Printing," *Multifunctional Materials* 1, no. 1 (2018): 015002.

28. "Frontal Polymerization," *Polymer Science: A Comprehensive Reference* (2012): 957–980.

29. M. G. Hennessy, A. Vitale, J. T. Cabral, and O. K. Matar, "Role of Heat Generation and Thermal Diffusion during Frontal Photopolymerization," *Physical Review E* 92, no. 2 (2015): 022403.

30. J. Warren, J. Cabral, and J. Douglas, "Solution of a Field Theory Model of Frontal Photopolymerization," *Physical Review E* 72, no. 2 (2005): 021801.

31. A. Vitale, M. G. Hennessy, O. K. Matar, and J. T. Cabral, "A Unified Approach for Patterning via Frontal Photopolymerization," *Advanced Materials* 27, no. 40 (2015): 6118–6124.

32. X. Kuang, J. Wu, K. Chen, et al., "Grayscale Digital Light Processing 3D Printing for Highly Functionally Graded Materials," *Science Advances* 5, no. 5 (2019): 5790.

33. S. P. Timoshenko and J. N. Goodier, *Theory of Elasticity*, 3rd ed. (McGraw-Hill, 1970).

34. Z. Li, Z. Liu, T. Y. Ng, and P. Sharma, "The Effect of Water Content on the Elastic Modulus and Fracture Energy of Hydrogel," *Extreme Mechanics Letters* 35 (2020): 100617.

35. V. V. Krongauz, "Diffusion in Polymers Dependence on Crosslink Density: Eyring Approach to Mechanism," *Journal of Thermal Analysis and Calorimetry* 102, no. 2 (2010): 435–445.

36. H. Tokuyama, Y. Nakahata, and T. Ban, "Diffusion Coefficient of Solute in Heterogeneous and Macroporous Hydrogels and Its Correlation with the Effective Crosslinking Density," *Journal of Membrane Science* 595 (2020): 117533.

37. J. Wang, X. Mu, D. Li, C. Yu, X. Cheng, and N. Dai, "Modeling and Application of Planar-to-3D Structures via Optically Programmed Frontal Photopolymerization," *Advanced Engineering Materials* 21, no. 5 (2019): 1801279.

38. C. Abhishek and N. Raghukiran, "Residual Stresses in 4D Printed Structures: A Review on Causes, Effects, Measurements, Mitigations, and Applications," *Forces in Mechanics* 18 (2025): 100304.

39. D. J. Glugla, M. D. Alim, K. D. Byars, et al., "Rigid Origami via Optical Programming and Deferred Self-Folding of a Two-Stage Photopolymer," *ACS Applied Materials & Interfaces* 8, no. 43 (2016): 29658–29667.

Supporting Information

Additional supporting information can be found online in the Supporting Information section.

Supporting file Supporting file